

pH-Dependent Behavior of Ionizable Cationic Lipids in mRNA-Carrying Lipoplexes Investigated by Molecular Dynamics Simulations

Giovanni Settanni,* Wolfgang Brill, Heinrich Haas, and Friederike Schmid*

Lipid-based nanoparticles and lipoplexes containing ionizable lipids are among the most successful nanocarriers for mRNA-based therapies. The molecular structure of these assemblies is still not fully understood, as well as the role played by the ionizable lipids. SAXS experiments have shown that lipoplexes including the ionizable lipid

2-dioleoyloxy-*N,N*-dimethyl-3-aminopropane (DODMA), under specific conditions, have a lamellar structure, where lipid bilayers are separated by mRNA-rich layers, with an overall spacing between 6.5 and 8.0 nm and a complex pH-dependence. Here, the structure and dynamics of these lipoplexes are investigated at varying pH and mRNA concentration using multiscale molecular dynamics simulations. It is observed that the interaction between DODMA and RNA is slightly attractive only at low pH levels, while it becomes effectively repulsive at high and intermediate pH. This results into a pH-dependent relocation of the RNA inside the multilayers, from the lipid head groups at low pH to a more uniform distribution inside the hydrophilic slabs of the multilayers at high pH. It is also observed that at high pH, DODMA lipids shift toward the hydrophobic part of the bilayer, consequently increasing their leaflet-flipping rate, a phenomenon which may ultimately affect the fusion process of the lipoplex with the endosomal membrane.

especially in the case of nucleic-acid-based therapies, like gene therapy, siRNA-mediated gene silencing, and mRNA-mediated immunotherapy (i.e., as for Covid-19 vaccines^[1,2]). Due to the large charge of nucleic acids, specific vectors must be designed which are capable of both protecting them from fast degradation and scuttling them across the membranes to let them reach the cellular compartments where they will carry out their function (gene insertion, silencing, expression, etc.). Lipoplexes and LNPs generally consist of a mixture of lipids including positively charged or ionizable cationic lipids, which have the role of interacting specifically with the negatively charged nucleic acids. Lipid-based delivery systems generally have fewer side effects than more traditional vectors like viruses. However, the efficiency of the whole transport and delivery process, the so-called transfection efficiency, that is a proxy of the amount of genetic material successfully expressed, is generally lower than viral vectors. In the last years, large


1. Introduction

Lipid-based materials like liposomes, lipoplexes, and lipid-based nanoparticles (LNP) represent fundamental drug delivery tools,

efforts have been undertaken to study and identify more efficient and less toxic lipid formulations for the assembly of lipid based delivery systems.^[3–5] These efforts have led to narrow down the range of variability of the lipid formulations, which, nowadays generally include the cationic/ionizable lipid, cholesterol, a helper lipid (typically a zwitterionic phospholipid like DOPE and DOPC), and a PEGylated lipid/molecule. The cationic/ionizable lipid represents a key component of the formulation, and small changes in its chemical structure may lead to large changes in transfection efficiency. A systematic evaluation of ionizable lipid libraries with respect to in vitro and in vivo transfection efficiencies^[3] has helped to identify some criteria that are essential for successful transfection. Nevertheless, an understating of the process, which involves a multitude of steps (nucleic acid encapsulation, nanoparticle fusion to endosomal membrane, nucleic acid endosomal escape, just to name few) is still missing.

The way nucleic acids are encapsulated in lipid based systems determines both the level of protection against degradation from the host organism, and the way nucleic acids will escape the endosome after the fusion of the nanoparticle with the endosomal membrane. SANS and SAXS experiments, as well as electron microscopy, reveal that lipoplexes, and to a lower extent, LNPs, show

G. Settanni, F. Schmid
 Department of Physics
 Johannes-Gutenberg University
 Staudingerweg 7, Mainz 55099, Germany
 E-mail: settanni@uni-mainz.de; friederike.schmid@uni-mainz.de
 W. Brill, H. Haas
 BioNTech SE
 An der Goldgrube 12, Mainz 55131, Germany

 The ORCID identification number(s) for the author(s) of this article can be found under <https://doi.org/10.1002/marc.202100683>

© 2021 The Authors. *Macromolecular Rapid Communications* published by Wiley-VCH GmbH. This is an open access article under the terms of the Creative Commons Attribution-NonCommercial-NoDerivs License, which permits use and distribution in any medium, provided the original work is properly cited, the use is non-commercial and no modifications or adaptations are made.

DOI: 10.1002/marc.202100683

a varying amount of lamellar structure (LNPs also show disordered inverse hexagonal phases under some conditions^[6]), where lipid bilayers are separated by nucleic-acid-rich regions.^[5–9] This identifies stacked lipid bilayers intercalated by nucleic-acid-rich regions as a fundamental component of these lipid-based materials. A recent study of formulations based on the ionizable cationic lipid DLin-KC2-DMA (KC2) and POPC under different pH conditions, using a combination of atomistic molecular dynamics (MD) simulations, NMR, SAXS, and cryo-EM,^[10] showed that KC2 and POPC have a tendency to segregate at high pH. In particular, the simulations suggest that the unprotonated KC2 may tend to be confined in the hydrophobic region between two phospholipid leaflets, and more in general, that the oil-like droplets observed in the core of LNP^[8,11] is rich in ionizable lipids. Atomistic molecular dynamics simulations^[12] of the complexation of RNA with a ionizable lipid-like agent (DML) provided information about the structural features of the complex, as well as the dynamics of the complexation process. Several coarse-grained models of lipoplexes and LNPs based on the MARTINI model and force field^[13,14] have been proposed in the past which showed a phase behavior comparable with experiments.^[11,15] Recently, coarse-grained simulations of the fusion process of lipoplexes and model membranes^[16] using the MARTINI force field, showed how the efficiency of the transfection process depends on the size and composition of the nanoparticle, as well as the composition of the receiving membrane. So far, using molecular dynamics simulations, we have addressed the interactions of polyanions, like nucleic acids, with polycations like polylysine-forming polyplexes,^[17] as well as the interactions between blood proteins and polymeric coatings of nanoparticles, like PEG, polyphosphoesters, and polysarcosine.^[18–20]

Here, we use a multiscale simulation approach to provide a detailed molecular picture of the internal structure of a lipoplex as a function of pH. A minimal lipoplex model is built by periodically stacking a lipid bilayer and the surrounding hydrophilic slab, along the direction orthogonal to the bilayer, with a periodicity matching the experimentally observed lamellar distances.^[9] In an initial step, we use a coarse grained (CG) representation of the system based on the MARTINI force field with polarizable water to build and relax the lipoplex structures on a time scale of several microseconds. These time scales, within the CG representation, are necessary to observe sufficient lateral diffusion of the various species along the bilayer plane. In a second step, we backmap the CG representations to an atomistic representations based on the CHARMM force field, which we use to obtain an accurate view of the structural and dynamical properties of the system on the 1 s time scale.

2. Results and Discussion

2.1. System Preparation and Simulations

A small portion of a lipoplex composed by 12.5%mol of DODMA (Figure 1a) and 87.5%mol of the helper lipid 1,2-dioleoyl-sn-glycero-3-phosphocholine (DOPC) was modeled as a bilayer containing 78 and 567 molecules of the two lipids, respectively, oriented normal to the Z direction. The lipid components of the system were chosen to reproduce the same experimental setup of ref. [9]. In that study, DOPC was chosen because it forms stable

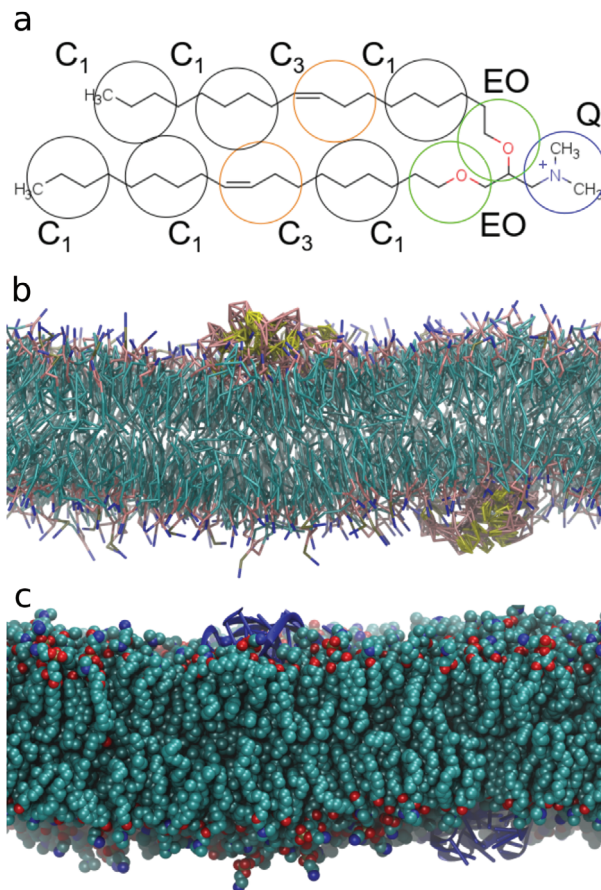


Figure 1. a) Chemical structure of protonated DODMA. The large circles identify the coarse-grained beads labeled with the corresponding MARTINI bead type. b) Coarse grained representation of the PORNA system after 4 μ s of coarse-grained simulations. The RNA stretches are rendered in yellow and pink, the lipid tails in cyan and the lipid heads in pink (phosphate group) and blue (amine and choline groups). Water beads are removed for clarity. c) The atomistic representation of the same system as in (b) after backmapping. RNA is rendered in blue; carbons, oxygen, and nitrogen atoms in the lipids are colored in cyan, red, and blue, respectively. Water molecules are removed for clarity.

lamellar phases above a temperature of 273 K, while other helper lipids may undergo phase transitions in the same range of temperatures. pH level was modeled by varying the amount of protonated DODMA lipids. Five different pH levels were considered with a DODMA protonation fraction α of 0%, 25%, 50%, 75%, and 100%, respectively. Five additional systems were also prepared by adding two RNA 40 mers close to the top and to the bottom leaflet of the bilayer to obtain an N/P ratio of 1. The RNA sequence was chosen randomly from a distribution of nucleotides biased toward the distribution used in a luciferase-translating mRNA optimized for maximal translation.^[21,22] The choice was intended to limit secondary structure formation, and resulted in a composition of 8, 11, 11, and 10 nucleotides of uridine, cytosine, adenine, and guanosine, respectively. The initial RNA structure was computed using MC-Fold.^[23] The systems were built with periodic boundary conditions in all directions and hydrated by a water slab. The amount of water particles added to the system was such that the periodicity along the Z direction was 7.4 and

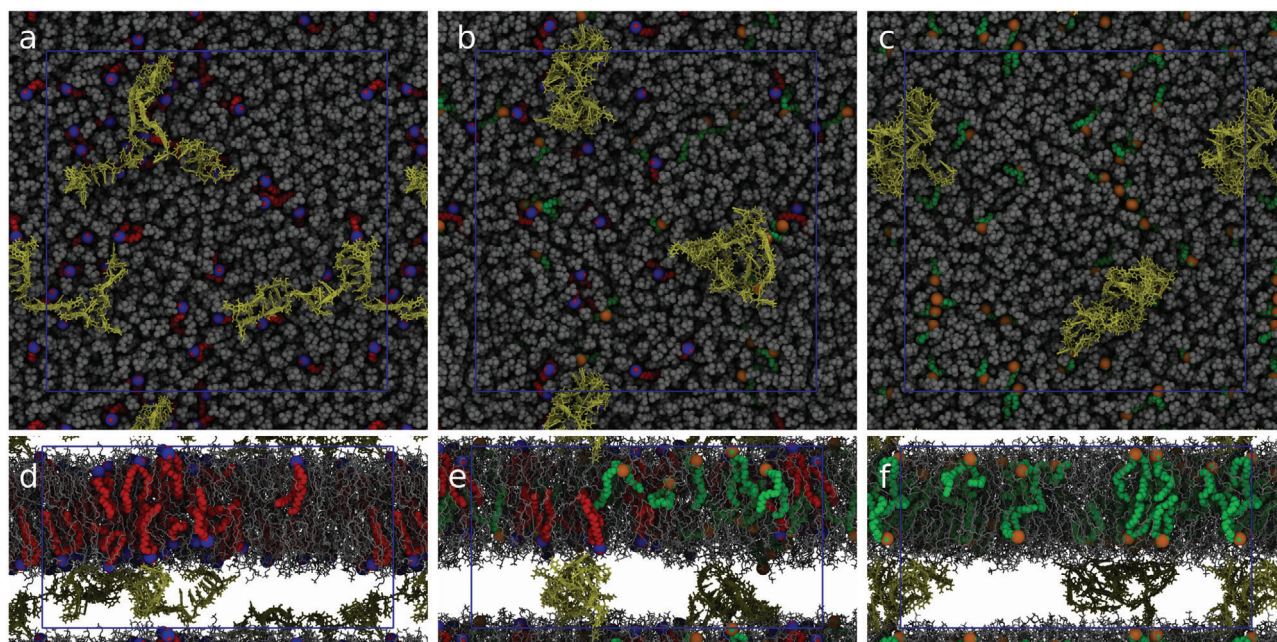


Figure 2. Conformations of the simulated systems after 1 μ s of atomistic simulations. In (a)–(c), a top view of the systems with a protonation fraction of 100%, 50%, and 0%, respectively, is displayed. Panels (d–f) report a front view of the same conformations. The RNA is represented as yellow licorice sticks on top of a cartoon representation to follow the backbone. DOPC lipids are represented in grey, protonated DODMA in red with blue nitrogen, neutral DODMA in green with light orange nitrogen. The blue square (top) and rectangle (bottom) represent the borders of the periodic box.

7.6 nm in the atomistic representation of the systems with and without RNA, respectively, in approximate agreement with the lamellar distance observed in SAXS data from ref. [9], with the aim of modeling the lamellar stack. In those experiments, long mRNA fragments were used which can very likely interact with both the upper and the lower leaflet of the water slab in which they are immersed inside the lipoplex. The length of the mRNA stretch chosen in the present work was sufficient to allow the observation of these interactions spanning across the water slab. The interaction of the RNA 40-mer with the upper leaflet of the bilayer on one side and with the periodic image of the lower leaflet on the other is not supposed to introduce significant artifacts because of the large thickness of the bilayer which extends over 4 nm and because the lipids are in the liquid disordered phase (as reported below by the tail order parameters, see below), thus helping decouple the upper and lower leaflet behavior. Sodium and chlorine counterions were added only to neutralize the systems, when necessary, considering that each RNA stretch has a charge of $-39e$ due to the phosphate groups and each protonated DODMA molecule has a $+1e$ charge.

The systems were initially simulated for 4 μ s using the MARTINI coarse-grained representation with the polarizable water model (see details in Section 4). Diffusion in coarse-grained simulations of this kind occurs approximately four times faster than in the equivalent atomistic systems^[14]; thus, the effective length of the simulations has to be considered proportionally larger than the nominal length reported above. The coarse-grained simulations are necessary to ensure proper mixing of the various lipid species in the bilayers, as well as around the RNA molecules, phenomena which would be very expensive to simulate using an atomistic representation. However, DODMA is relatively different from the lipids that have been used to benchmark the MAR-

TINI model and the standard bead types available in MARTINI may not be able to reproduce DODMA behavior with large accuracy, especially addressing the differences between charged and uncharged species. Similar modeling inaccuracies have been indeed already reported for the cationic lipid DOTAP.^[15] In addition, the MARTINI model of RNA has been benchmarked by constraining the tertiary structure with elastic networks. Atomistic simulations, on the other hand, allow to model significantly more precisely the differences between neutral and protonated DODMA, thanks to the large database of chemical species already parameterized and the CHARMM-gui^[24–26] software which allows for extending the parameterization to slightly different molecules. In addition, although possibly not accurate enough for RNA folding studies, atomistic approaches allow modeling RNA interactions and, to some extent, flexibility, within the limits imposed by the force field and the length scales of the simulations, keeping in mind that the focus of the present work is not RNA dynamics. For these reasons, after completing the coarse grained simulations, we backmapped the conformations of the systems to an atomistic representation (Figure 1b,c). The atomistic representations of the systems were simulated for 1 μ s (see Section 4 for the simulation details) and the generated trajectories were analyzed. In Figure 2, the conformations of some of the systems at the end of the atomistic simulations are reported.

2.2. DODMA Location and Orientation in the Bilayer is a Function of pH

The density of the various chemical species along the normal of the bilayer was averaged across the simulations (Figure 3). These data reveal that, while the position of DOPC phosphate

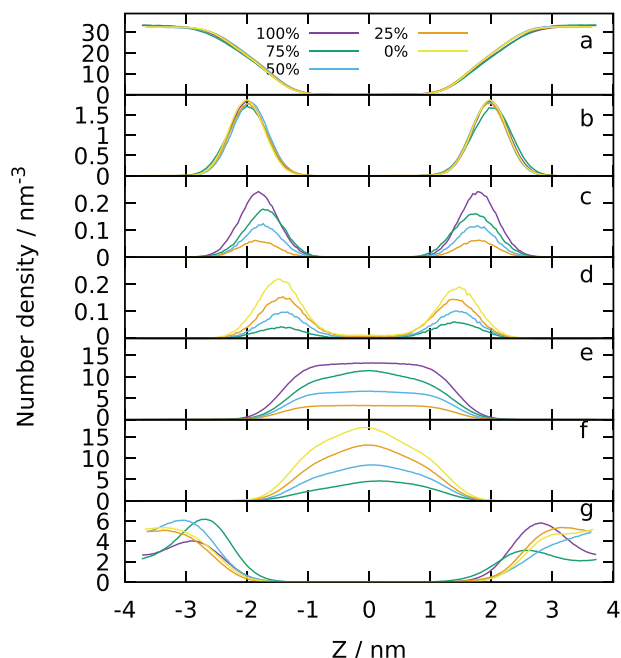


Figure 3. The average number density along the normal to the bilayer of water (a), phosphate atom of DOPC (b), nitrogen atom of charged DODMA (DODMA_p) (c) and neutral DODMA (DODMA_0) (d), tail carbon atoms of DODMA_p (e) and DODMA_0 (f), and heavy atoms of RNA (g) are reported. The color of the lines reports the protonation α of DODMA as indicated by the legend.

groups is relatively unaffected by the change of pH (that is by the amount of protonated DODMA in the simulation box), the latter has an effect on the average position of the DODMA molecules in the bilayer. Indeed, protonated and neutral DODMA molecules (DODMA_p and DODMA_0 , respectively) behave quite differently: the DODMA_p head density shows a peak about 0.2 nm deeper in the membrane than the DOPC phosphate, while, for DODMA_0 , the peak reaches 0.5 nm deeper than DOPC phosphate into the membrane. This effect is related to the different hydrophilicity of DODMA's head dependent upon its protonation state. The head of DODMA_0 can penetrate deep into the lipid tail region, indicating a relatively low barrier to lipid flipping (Figures 4a and 5a) of about 2 Kcal/mol (8.4 KJ/mol). Considering both charged and uncharged DODMA, this indicates that the free energy barrier to lipid flipping is pH dependent (Figures 4b and 5b).

Lipid flipping between upper and lower leaflets of membrane bilayers is a phenomenon which occurs generally on long time scales, due to the large free energy barrier associated to the need of the polar head crossing the large hydrophobic region of the lipid tails. This is not the case for neutral DODMA, whose head is less hydrophilic than charged DODMA as documented above by the pH-dependent height of the free energy barrier to flipping (Figure 4). We observed that neutral DODMA lipids, unlike DOPC or charged DODMA, undergo several flipping events during 1 μs of atomistic simulations (see Section 4 for the definition of flipping events). The number of events observed is roughly proportional to the number of neutral lipids present in the simulation (Figure 6). The flipping events seem uncorrelated: Most lipids flip at most once during the simulation time (data not

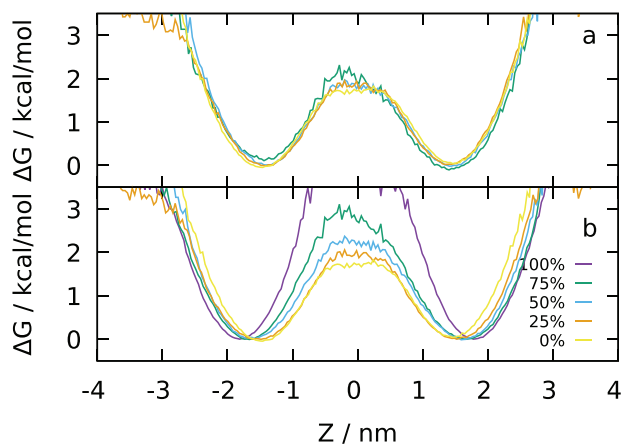


Figure 4. Projection along the normal to the bilayer of the free energy surface of the nitrogen atom of neutral DODMA (DODMA_0) (a) and of any DODMA molecule (b). The color of the lines reports the protonation α of DODMA as indicated by the legend. In these simulations, RNA is included.

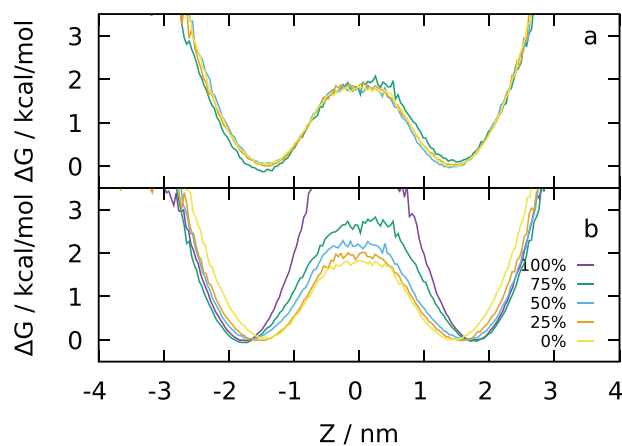


Figure 5. Same as 4 but for the simulations without RNA.

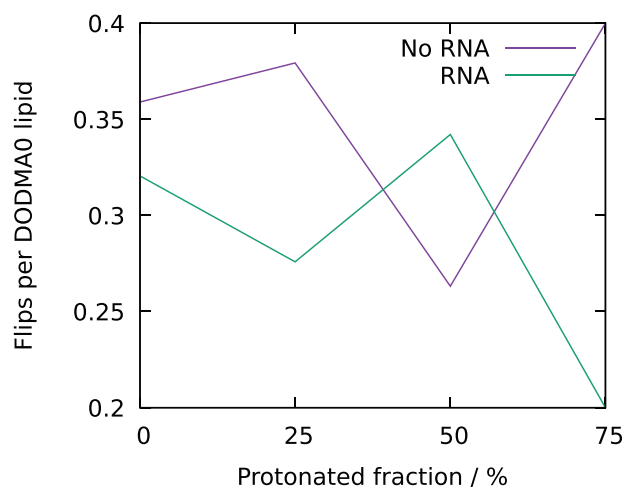


Figure 6. Number of lipid flipping events per neutral DODMA lipid observed along 1 μs of atomistic simulations as a function of the protonated fraction of DODMA. The number of flips per lipid does not change significantly with DODMA protonated fraction; thus, the total number of observed flips in a simulation is proportional to the number of neutral DODMA lipids.

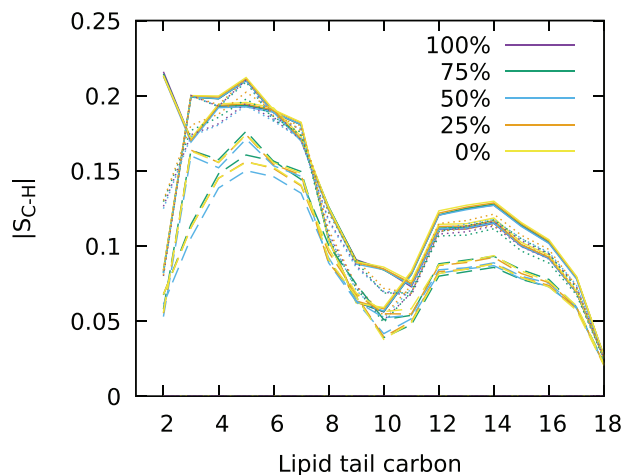


Figure 7. Tail order parameters for DOPC (solid line), DODMA_p (dotted line), and DODMA₀ (dashed line). The color of the lines report the protonation α of DODMA as indicated by the legend. Simulations including RNA are reported. The values for sn1 and sn2 chains are both reported.

shown). In the rare instances where a lipid flipped twice, forth and back between leaflets, the time between the two events was never shorter than few ns.

Beside the head group position, also the density of the tail carbons of DODMA_p and DODMA₀, shows notable differences (Figure 3). While DODMA_p tail atoms occupy uniformly the hydrophobic part of the membrane, DODMA₀ tails tend to accumulate in the very middle of the membrane. In addition to that, while the tail order parameters, measured as explained in Section 4, are very close to one another for DODMA_p and DOPC (Figure 7) and indicate a significant alignment of the lipid tails to the normal of the bilayer, the DODMA₀ tail order parameters are significantly lower, indicating partial or temporary loss of alignment for these lipids.

An accumulation of the ionizable cationic lipid KC2 between the two phospholipid leaflets was observed in previous simulations.^[10] Neutral KC2 has most probably a less hydrophilic footprint than DODMA₀ due to the presence of the bulkier dioxolane group in the lipid head. This may explain why we observe only a decrease of the free energy barrier to leaflet flipping, but not an accumulation of DODMA in the mid-membrane plane. The results of these studies, taken together, suggest that fine-tuning the chemical structure of the head group of the ionizable lipid may help regulate the height of the free energy barrier to lipid flipping as a function of pH.

We note that, no significant dependence on pH (protonation) or on RNA presence is observed for the density peaks position and width of P, N0, or NP (Figure 8) or water half-bulk-density coordinates (Figure 3a). This indicates that the thickness of the bilayer remains approximately constant in the simulations. This is not in contrast with the experimental data in ref. [9], where a change in the lamellar spacing of the lipoplex is observed as a function of pH. The lamellar spacing (which, in the simulations, is the spacing between a bilayer and its periodic image along the Z direction) is determined mostly by the amount of water separating the bilayers. This amount was fixed at the beginning of the

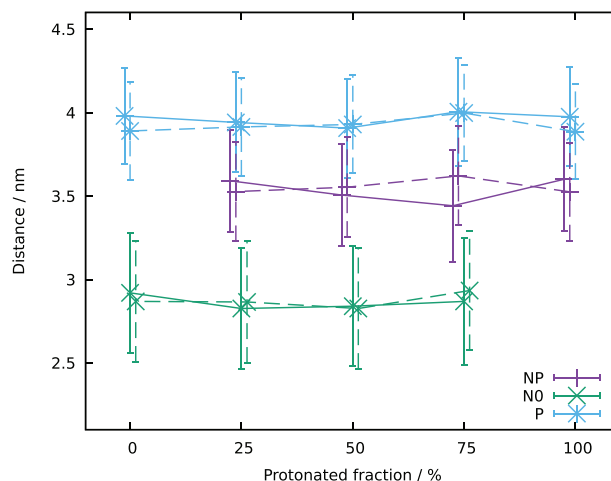


Figure 8. The density peaks in Figure 3 where fitted to Gaussian functions. The distance between the mean in the lower and upper leaflet are reported, along with their width (as error bar), as a function of the protonated fraction of DODMA. The data for the nitrogen atoms of protonated and neutral DODMA (NP and N0) and for the phosphate atom (P) of DOPC are rendered in purple, green, and light blue, respectively. Data from the simulations with RNA (solid line) as well, without RNA (dashed lines) are reported.

simulation to give approximately the same spacing in all simulations and cannot change during their course.

2.3. DODMA Interactions with RNA are Strongly pH Dependent

Already a visual inspection of the simulations (Figure 2) shows that charged DODMA (DODMA_p) tends to accumulate around the RNA molecule. The density profiles (Figure 3g) show that RNA accumulates on the bilayer surface at low pH (i.e., high protonation level) and goes to the middle of the water slab in high pH simulations. We quantified this tendency more precisely by measuring the excess of DODMA molecules found in the vicinity of RNA, and associating it with a binding free energy:

$$\begin{aligned} \Delta G_{\text{DODMA}} &= -RT \log \left(\frac{[\text{DODMA}]_{\text{RNA}}}{[\text{DODMA}]_{\text{unbound}}} \right) \\ &= -RT \log \left(\frac{\frac{N_p + N_0}{N_p + N_0 + N_{PC}}}{\frac{T_D - N_p - N_0}{T_I - N_p - N_0 - N_{PC}}} \right) \end{aligned} \quad (1)$$

$$\begin{aligned} \Delta G_{\text{DODMA}_p} &= -RT \log \left(\frac{[\text{DODMA}_p]_{\text{RNA}}}{[\text{DODMA}_p]_{\text{unbound}}} \right) \\ &= -RT \log \left(\frac{\frac{N_p}{N_p + N_0 + N_{PC}}}{\frac{T_D - N_p}{T_I - N_p - N_0 - N_{PC}}} \right) \end{aligned} \quad (2)$$

Here, N_p , N_0 , N_{PC} are the number of DODMA_p, DODMA₀, and DOPC molecules, respectively, with at least a heavy atom within 0.7 nm of any RNA atom, and T_I and T_D are the total number of lipids and DODMA molecules, respectively, in the

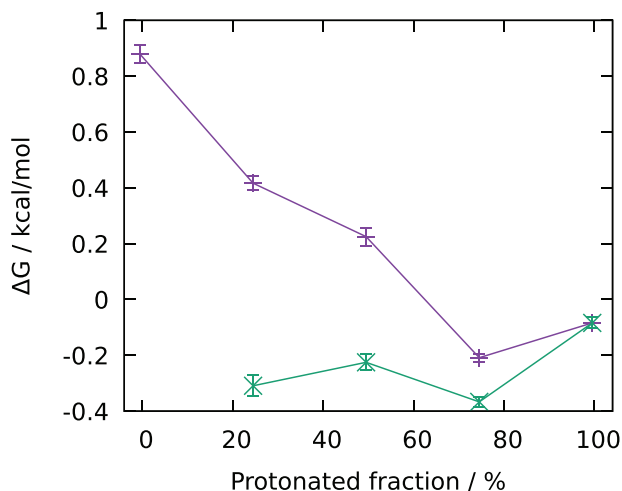


Figure 9. The free energy of binding ΔG_{DODMA} of DODMA to the RNA molecules (Equation (1)) is reported as a function of DODMA protonated fraction (purple line). The green line reports the $\Delta G_{\text{DODMA}_p}$ of the protonated DODMA molecules only (Equation (2)).

simulation box. Although the simulations show an initial drift in the instantaneous binding free energy (data not shown), by excluding the first 300 ns of the simulation from the analysis, block averaging of the data shows a substantial convergence of Equation (2) to values in the interval $[-0.3; -0.1]$ Kcal mol⁻¹ ($[-1.3; -0.4]$ KJ mol⁻¹) for DODMA_p (Figure 9), independent from pH (only the charged molecule is considered). Considering instead all DODMA molecules independent of protonation (i.e., both charged and neutral, Equation (1)), we obtain a pH-dependent binding constant that is negative at low pH and becomes positive for a fraction of protonated DODMA equal or smaller than 50%, reaching a value close to +0.9 Kcal mol⁻¹ (3.8 KJ mol⁻¹) at very high pH (Figure 9).

The enhanced interactions between DODMA and RNA at low pH has consequences on the lateral diffusion of the involved molecules. RNA diffusion occurs tendentially faster at high pH as indicated by the larger lateral mean square displacement (MSD) of the molecules (Figure 10a), that is, when RNA is not pinned to the membrane by the interactions with charged DODMA. Furthermore, RNA's presence slows down slightly the diffusion of DODMA, in most of the simulated conditions, with the exception of the 100% protonated DODMA simulation (Figure 10b,c). On the contrary, the presence of RNA does not affect systematically the diffusion of DOPC (Figure 10d). No significant difference in diffusion between charged and uncharged DODMA in the presence of RNA nor in its absence are observed (Figure 10b,c). Details about the MSD calculations are reported in Section 4.

The binding of DODMA to RNA at low pH results in overall structural changes in RNA. We calculated the exposed surface of the lipid membrane, the RNA molecules as well as the complex formed by the binding of RNA to the membrane. The calculations show that the RNA surface area (SA) decreases with rising pH and reaches a plateau at a pH where 50% of ionizable lipids are protonated. This indicates that RNA swells at low pH while it has a more compact structure at high pH (Figure 11a). The RNA surface buried by the contact with the membrane is also higher at low pH, with a similar trend as for the total RNA SA. The frac-

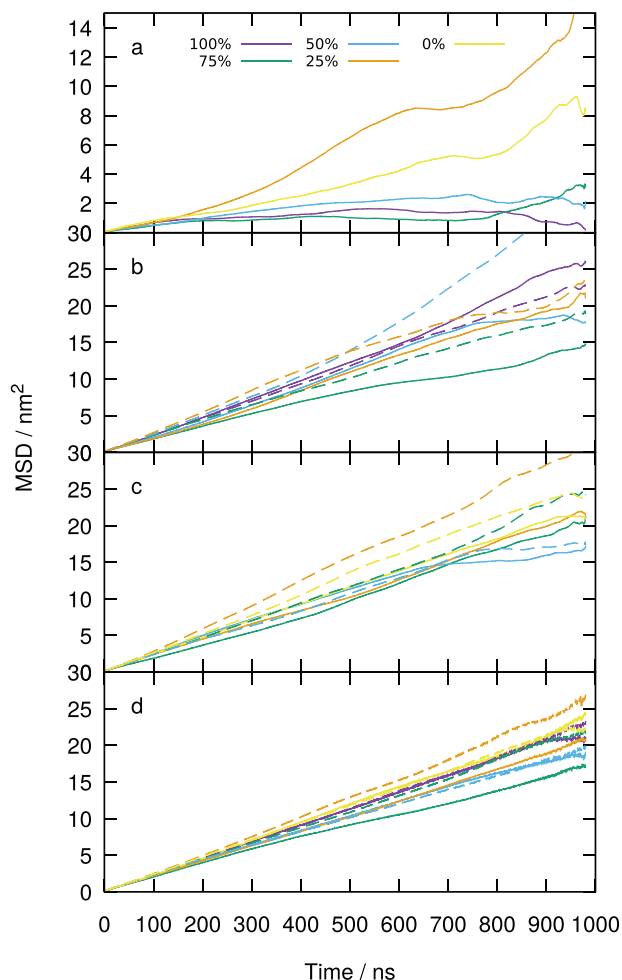


Figure 10. The time dependence of the mean squared displacement (MSD) of a) RNA, b) charged DODMA, c) neutral DODMA, and d) DOPC is reported for simulations with RNA (solid line) and without it (dashed line).

tion of accessible surface area of the RNA, decreases slightly with decreasing pH (Figure 11b,d). In addition, we observed that the presence of RNA does not significantly affect the overall SA of the lipid bilayer (Figure 11c). The latter increases weakly with pH, probably due to a change in roughness of the lipid surface in the presence of ionized lipids.

2.4. Hints to a pH-Dependent Lateral Phase Separation

We monitored the density distribution of the nitrogen atom of DODMA along the two leaflets of the bilayer, separately (see Section 4 for details). The data show that while neutral DODMA lateral density distribution is unaffected by the presence of RNA, charged DODMA shows a much broader lateral density distribution in the presence of RNA than without it especially at high and intermediate protonation fraction (Figure 12). The phenomenon is related to charged DODMA lipids accumulating around the RNA molecules thus leading to the formation of highly populated regions around the RNA and low populated regions away from it, as also visible in Figure 2a,d. At very high protonation level,

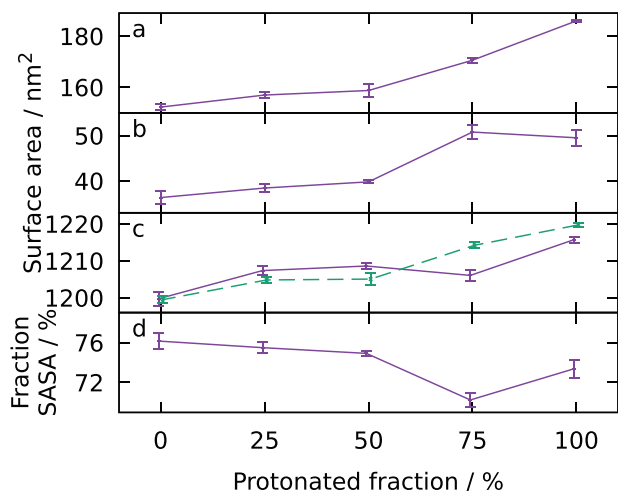


Figure 11. Dependence on pH (i.e., protonation fraction) of a) the total surface area of the RNA molecules; b) the RNA surface area buried by membrane contacts; c) the surface area of the bilayer in the simulations with RNA (purple solid line) and without RNA (green dashed line); d) the fraction of solvent exposed surface of RNA.

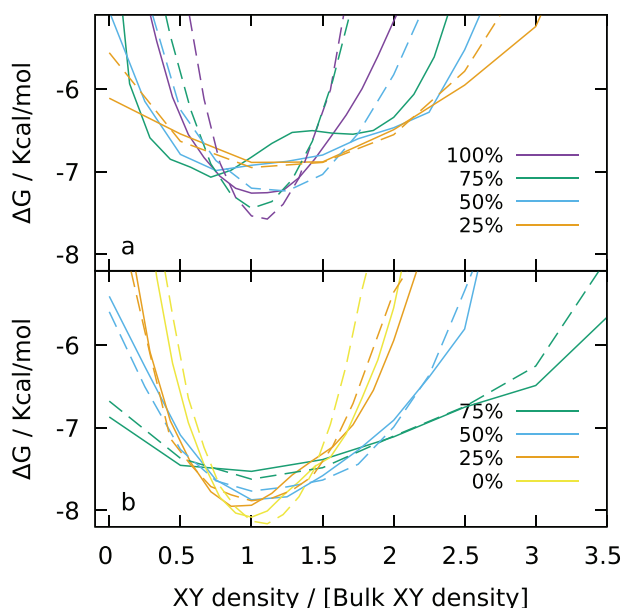


Figure 12. Projection of the free energy of the system along the local density of DODMA_p a) and DODMA₀ b) molecules along the XY plane, computed separately for the two leaflets. Solid and dashed lines report the profile for simulations with and without RNA, respectively. The color of the lines reports the fraction of protonated DODMA molecules in the simulation as indicated in the legend.

the lateral distribution of lipids in the presence of RNA seems to become more homogeneous than at high and intermediate protonation because the RNA molecule occupies a larger surface on the bilayer, as evidenced by the surface area calculations exposed above. The contrasting results obtained at intermediate-high and very high protonated DODMA fraction do not allow to make conclusive statements on emergence of a lateral phase separation caused by the binding of protonated DODMA with RNA.

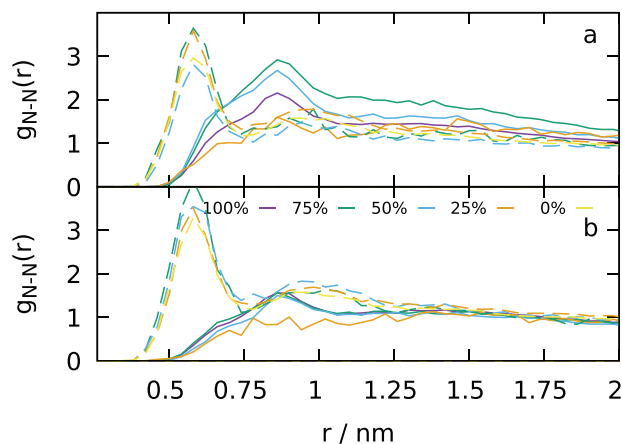


Figure 13. The radial distribution function of the N-N distance of DODMA_p (solid line) and DODMA₀ (dashed line). The data from the simulations with RNA a) and without it b) are reported. The color of the lines reports the fraction of protonated DODMA molecules in the simulation as indicated in the legend.

In addition, we observed that the radial distribution function ($g_{N-N}(r)$) of the nitrogen-nitrogen distance of DODMA₀ molecules has a pronounced peak at around 0.6 nm (Figure 13) unlike DODMA_p, whose peak is broader and located almost at 0.9 nm. This indicates the tendency of DODMA₀ molecules to cluster with each other, as it can also be visually observed in Figure 2c, where two four-molecule clusters are formed. This tendency however does not result in an evident lateral phase separation according to the density analysis provided above, possibly due to the longer time scales/larger systems needed to observe the phenomenon. The peaks of the $g_{N-N}(r)$ do not shift neither as a function of the presence of the RNA nor of the pH (DODMA protonation). However, the height of the DODMA_p peak is strongly pH dependent in the presence of RNA (Figure 13a), supporting the observation of the formation of broad DODMA_p patches interacting with RNA.

3. Conclusion

The MD simulations presented here help elucidate several aspects characterizing DODMA-based nanoparticles for mRNA delivery. On one hand they show that in the lamellar structure formed by an alternation of lipid bilayer and nucleic acid, the RNA-DODMA interactions are weakly attractive only at low pH, while at high pH they become mostly repulsive. This has an effect on the overall structure and location of RNA within the lamellar phase: at low pH RNA is pulled by DODMA to the surface of the lipid bilayer. The pull exerted by the two opposite bilayer surfaces on a stretch of RNA affects the structure of the biopolymer which becomes more extended than at high pH, as reported by its increased surface area. Another important aspect revealed by the present simulations is the role played by DODMA molecules in the lamellar structure of the nanoparticle. At low pH, they behave similarly to a phospholipid with the charged head exposed on the surface of the bilayer, while at high pH DODMA molecules occupy a deeper position inside the bilayer and the barrier to lipid flipping decreases significantly, although unlike KC2 ionizable

Table 1. List of the simulations.

	RNA	DODMA Protonation (%)	DOPC / DODMA _p / DODMA ₀	Coarse-grained simulations			Atomistic simulations		
				Box size [nm]	No. Beads	Length (μs)	Box size [nm]	No. Atoms	Length (μs)
P0	no	100	567 / 78 / 0	15 × 15 × 7	27936	4	14.5 × 14.5 × 7.6	169338	1
P1	"	75	" / 58 / 20	"	27930	"	"	169274	"
P2	"	50	" / 38 / 38	"	27905	"	"	168972	"
P3	"	25	" / 20 / 58	"	27933	"	"	169210	"
P4	"	0	" / 0 / 78	"	27915	"	"	169098	"
PORNA	yes	100	" / 78 / 0	15 × 15 × 7	26617	"	14.5 × 14.5 × 7.4	164380	"
P1RNA	"	75	" / 58 / 20	"	26632	"	"	164440	"
P2RNA	"	50	" / 38 / 38	"	26610	"	"	164190	"
P3RNA	"	25	" / 20 / 58	"	26617	"	"	164380	"
P4RNA	"	0	" / 0 / 78	"	26569	"	"	164188	"

cationic lipids,^[10] they do not segregate inside the bilayer. The pH-dependent intra and inter-leaflet mobility of DODMA may play a role during the fusion process with the endosomal membrane, in addition to the degree of saturation of the lipid tails reported in ref. [16]. Based on the setup presented here, the simulations help clarify the local structure and dynamics of the lamellar phase of the lipoplex on a length scale comparable to the lamellar distance (about 7 nm^[9]). In LNPs, the lamellar structure is not as well defined as in lipoplexes and its appearance is dependent on the environmental conditions.^[6] Nevertheless, under the conditions where a lamellar phase appears, the local structure and dynamics should follow a trend similar to the one described here. Overall, the accurate insight into the pH-dependent molecular rearrangements observed in the models of ionizable-lipid-based mRNA-delivery systems studied here may allow for a more accurate tailoring of their behavior in circulation, cellular uptake, and endosomal processing.

4. Experimental Section

Coarse-Grained Simulations: The simulations were carried out using the program GROMACS 2020.1.^[27–30] The program INSANE^[31] was used to build a coarse-grained (CG) representation of the systems using the MARTINI force field.^[14,32–34] The MARTINI polarizable water model^[35] was adopted which allows for a more accurate treatment of the electrostatic interactions than standard MARTINI. For the DOPC molecules, the standard MARTINI force field was used, while DODMA was parameterized as follows: the bead type of the tails were copied from DOPC as they are chemically equivalent, the linker was modeled using two EO beads from the PEO/PEG MARTINI force field,^[34] and the head was assigned a Qd and Na bead type for protonated and neutral DODMA, respectively (Figure 1a). The Qd bead in protonated DODMA was assigned a +1e charge, while the Na bead in neutral DODMA has no charge. The angles involving the linker beads was adjusted to match the distribution observed in preliminary atomistic simulations (see below). The extension of MARTINI force field to RNA^[33] was used to model the RNA molecules. The resulting RNA model, although not adequate to studying the folding dynamics of the molecule, provides a way to address its interactions with the surrounding lipids and solvent. A cutoff of 1.2nm for both VdW and direct electrostatic interactions was adopted and PME^[36] was used for the long range electrostatics. Each system was subjected to energy minimization (10000 steps), followed by 5 ns of equilibration with a time step of 10 fs. During equilibration V-rescale^[37] and Berendsen^[38] algorithms were

adopted to keep temperature and pressure of the system constant at 300 K and 1 atm, respectively, with time coupling constants of 1 ps and 5 ps, respectively. The pressure coupling was semi-isotropic. The production was run for 4.0 μs with a 8 and 20 fs time step for the simulations with and without RNA, respectively. During production, the v-rescale^[37] and the Parrinello–Rahman^[39] algorithms were used to keep temperature and pressure constant at 300 K and 1 atm, respectively, with coupling constants of 1 and 12 ps, respectively. Pressure control was semi-isotropic in this case, as well. Figure 1b reports the final structure of the CG simulations of system PORNA.

Atomistic Simulations: The last frames of the coarse-grained simulations were backmapped to atomistic representations with the BACKWARD program^[40] (Figure 1c). The CHARMM 36 force field^[41–43] was adopted which provides parameters for all the component of the systems with the exception of DODMA. DODMA was modeled as follows: the parameters for the tails were taken from DOPC, while the ether linker region was modeled as in the ether lipid DHPC.^[44] The charged and neutral heads were modeled using CHARMM-gui^[24–26] and the CHARMM generalized force field.^[45] In particular, protonated DODMA has an additional proton, with respect to neutral DODMA, covalently bound to the nitrogen atom of the head and a +1e charge distributed on the atoms of the lipid head as determined by CHARMM-gui. Direct non-bonded interactions were cut off at 12 nm, while PME^[36] was used for long range electrostatics. Bonds involving hydrogen atoms were constrained with the P-LINCS algorithm.^[46] The system was minimized for a maximum of 50000 steps. Then, it was equilibrated in two steps at constant volume and constant temperature of 300 K using the v-rescale^[37] algorithm with a time constant of 0.1 ps. In the first step, a 50 ps simulation was run with a time step of 1 fs. This was followed by a second 200 ps run obtained with a 2 fs time step. The equilibration was then continued for 1 ns in the NPT ensemble with the Nose-Hoover^[47–49] temperature coupling with 300 K target temperature and 0.5 ps relaxation time and the Parrinello–Rahman^[39] semi-isotropic pressure coupling with 5 ps relaxation time and a target pressure of 1 atm. In the production runs, the same parameters as in the NPT equilibration phase were adopted, with the exception of the pressure relaxation time of 2 ps. These runs were extended for 1 μs; however, the first 25 ns were discarded from the analysis, to allow for a more thorough equilibration. Trajectory snapshots were saved every 0.4 ns for analysis. A list of the simulations performed including system description, resolution, size, and length is reported in Table 1.

Analysis: The reported analysis were carried out on the atomistic simulation trajectories. The visualization and rendering of molecular structures was done using VMD.^[50] Graphs were prepared using GNUPLOT.^[51] The program WORDOM^[52] and the python library MDAnalysis^[53,54] were used for the analysis.

The number density of the chemical groups along the normal of the bilayer (Figure 3) were computed after centering the terminal part of the tails

of the lipids in the simulation box so that their center of mass had the coordinate $Z = 0$ and using the GROMACS density tool. The projection of the free energy surface of the nitrogen atoms (Figures 4 and 5) were obtained by normalizing the number density to obtain the probability distribution $P(Z)$ of the selected atoms and defining $\Delta G(Z) = -k_b T \log P(Z)$.

Lipid flips were defined as follows: a lipid was considered to have reached the upper (lower) leaflet as soon as the nitrogen of the lipid reached the region with $Z > 2$ nm ($Z < -2$ nm) and did not flip back for the next 6 ns of trajectory to avoid counting irrelevant recrossings.^[55]

Tail order parameters were computed using the software made available by the NMRlipids project.^[56,57]

The density distribution of atoms along the Z direction was fitted with Gaussian separately for the upper and lower leaflet. The least-square fit was performed using GNUPLLOT.^[51]

The lateral MSD along the XY plane (parallel to the bilayer) was computed using the GROMACS utility "msd". The measure was obtained averaging over all the atoms of the molecules under consideration, as well as over the trajectory. No correction due to the finite size of the box was applied as the authors were only interested in the relative diffusivity of the molecules in simulations which share the same periodic box dimension.

The surface areas were computed using the GROMACS "sasa" utility. Also in this case, all the atoms of the molecules under consideration were used as input. The areas were computed for each trajectory frame and then block averaging was used to obtain the standard error on the average in Figure 10.

The distribution of the lipid densities along the XY plane was computed by splitting the periodic box side in the XY direction in four equal sub-boxes and counting the numbers D_{N_p} and D_{N_0} of nitrogen atoms of DODMA_p and DODMA₀ ending up in each sub-box, separately for each leaflet. A histogram of the D_{N_p} and D_{N_0} observed along the trajectory was built and normalized to obtain the probability $P(D_p)$ ($P(D_0)$) of observing those values. The free energy in Figure 12 is obtained as $\Delta G(D_{p/0}) = -k_b T \log(P(D_{p/0}))$.

Acknowledgements

The research was supported by the German Research Foundation (DFG) with the grants SFB1066 project Q1 and SFB-TRR146. The authors gratefully acknowledge support with computing time from the HPC facility Hawk at the High Performance Computing Center Stuttgart (HLRS) project Flexadfg and the HPC facility Mogon at the University of Mainz.

Open Access funding enabled and organized by Projekt DEAL.

Conflict of Interest

The authors declare no conflict of interest.

Data Availability Statement

The data that support the findings of this study are available from the corresponding author upon reasonable request.

Keywords

2-dioleoyloxy-*N,N*-dimethyl-3-aminopropane, ionizable lipids, lipoplex, molecular dynamics simulations, RNA delivery

Received: October 12, 2021

Revised: November 26, 2021

Published online: December 17, 2021

[1] F. P. Polack, S. J. Thomas, N. Kitchin, J. Absalon, A. Gurtman, S. Lockhart, J. L. Perez, G. P. Marc, E. D. Moreira, C. Zerbini, R. Bailey, K. A.

- Swanson, S. Roychoudhury, K. Koury, P. Li, W. V. Kalina, D. Cooper, J. Robert, W. Frenck, L. L. Hammitt, Ö. Türeci, H. Nell, A. Schaefer, S. Ünal, D. B. Tresnan, S. Mather, P. R. Dormitzer, U. Ahin, K. U. Jansen, W. C. Gruber, *NEJM* **2020**, *383*, 2603.
- [2] L. R. Baden, H. M. E. Sahly, B. Essink, K. Kotloff, S. Frey, R. Novak, D. Diemert, S. A. Spector, N. Roupheal, C. B. Creech, J. McGettigan, S. Khetan, N. Segall, J. Solis, A. Brosz, C. Fierro, H. Schwartz, K. Neuzil, L. Corey, P. Gilbert, H. Janes, D. Follmann, M. Marovich, J. Mascola, L. Polakowski, J. Ledgerwood, B. S. Graham, H. Bennett, R. Pajon, C. Knightly, et al., *NEJM* **2020**, *384*, 403.
- [3] K. A. Whitehead, J. R. Dorkin, A. J. Vegas, P. H. Chang, O. Veiseh, J. Matthews, O. S. Fenton, Y. Zhang, K. T. Olejnik, V. Yesilyurt, D. Chen, S. Barros, B. Klebanov, T. Novobrantseva, R. Langer, D. G. Anderson, *Nat. Commun.* **2014**, *5*, 4277.
- [4] M. R. Molla, S. Chakraborty, L. Munoz-Sagredo, M. Drechsler, V. Orian-Rousseau, P. A. Levkin, *Bioconjug. Chem.* **2020**, *31*, 852.
- [5] Y. Eygeris, S. Patel, A. Jozic, G. Sahay, G. Sahay, *Nano Lett.* **2020**, *20*, 4543.
- [6] M. Y. Arteta, T. Kjellman, S. Bartesaghi, S. Wallin, X. Wu, A. J. Kvist, A. Dabkowska, N. Székely, A. Radulescu, J. Bergenholtz, L. Lindfors, *Proc. Natl. Acad. Sci. U. S. A.* **2018**, *115*, E3351.
- [7] A. Ziller, S. S. Nogueira, E. Hühn, S. S. Funari, G. Brezesinski, H. Hartmann, U. Sahin, H. Haas, P. Langguth, *Mol. Pharm.* **2018**, *15*, 642.
- [8] J. A. Kulkarni, M. M. Darjuan, J. E. Mercer, S. Chen, R. van der Meel, J. L. Thewalt, Y. Y. C. Tam, P. R. Cullis, *ACS Nano* **2018**, *12*, 4787.
- [9] L. Uebbing, A. Ziller, C. Siewert, M. A. Schroer, C. E. Blanchet, D. I. Svergun, S. Ramishetti, D. Peer, U. Sahin, H. Haas, P. Langguth, *Langmuir* **2020**, *36*, 13331.
- [10] M. Ramezanpour, M. L. Schmidt, I. Bodnariuc, J. A. Kulkarni, S. S. W. Leung, P. R. Cullis, J. L. Thewalt, D. P. Tieleman, *Nanoscale* **2019**, *11*, 14141.
- [11] A. K. K. Leung, I. M. Hafez, S. Baoukina, N. M. Belliveau, I. V. Zhigaltsev, E. Afshinmanesh, D. P. Tieleman, C. L. Hansen, M. J. Hope, P. R. Cullis, *J. Phys. Chem. C* **2012**, *116*, 18440.
- [12] A. N. Rissanou, A. Ouranidis, K. Karatasos, *Soft Matter* **2020**, *16*, 6993.
- [13] S. J. Marrink, A. H. de Vries, A. E. Mark, *J. Phys. Chem. B* **2004**, *108*, 750.
- [14] S. J. Marrink, H. J. Risselada, S. Yefimov, D. P. Tieleman, A. H. De Vries, *J. Phys. Chem. B* **2007**, *111*, 7812.
- [15] J. Corsi, R. W. Hawtin, O. Ces, G. S. Attard, S. Khalid, *Langmuir* **2010**, *26*, 12119.
- [16] B. M. Bruininks, P. C. Souza, H. Ingolfsson, S. J. Marrink, *Elife* **2020**, *9*, e52012.
- [17] P. Heller, J. Zhou, B. Weber, D. Hobernik, M. Bros, F. Schmid, M. Barz, *Small* **2017**, *13*, 1603694.
- [18] G. Settanni, J. Zhou, T. Suo, S. Schöttler, K. Landfester, F. Schmid, V. Mailänder, *Nanoscale* **2017**, *9*, 2138.
- [19] G. Settanni, J. Zhou, F. Schmid, *J. Phys. Conf. Ser.* **2017**, *921*, 012002.
- [20] G. Settanni, T. Schäfer, C. Muhl, M. Barz, F. Schmid, *Comput. Struct. Biotechnol. J.* **2018**, *16*, 543.
- [21] A. G. Orlandini von Niessen, M. A. Poleganov, C. Rechner, A. Plaschke, L. M. Kranz, S. Fesser, M. Diken, M. Löwer, B. Vallazza, T. Beissert, V. Bukur, A. N. Kuhn, Ö. Türeci, U. Sahin, *Mol. Ther.* **2019**, *27*, 824.
- [22] A. G. Orlandini von Niessen, S. Fesser, B. Vallazza, T. Beissert, A. N. Kuhn, U. Sahin, M. A. Poleganov 3' Utr Sequences For Stabilization Of Rna, 2017, Patent WO2017/060314A3 <https://patents.google.com/patent/WO2017060314A3/en>. Accessed 12/2021.
- [23] M. Parisien, F. Major, *Nat.* **2008** *452*7183 **2008**, *452*, 51.
- [24] S. Jo, T. Kim, V. G. Iyer, W. Im, *J. Comput. Chem.* **2008**, *29*, 1859.
- [25] J. Lee, X. Cheng, J. M. Swails, M. S. Yeom, P. K. Eastman, J. A. Lemkul, S. Wei, J. Buckner, J. C. Jeong, Y. Qi, S. Jo, V. S. Pande, D. A. Case, C. L.

- Brooks, A. D. MacKerell, J. B. Klauda, W. Im, *J. Chem. Theory Comput.* **2016**, *12*, 405.
- [26] S. Kim, J. Lee, S. Jo, C. L. Brooks, H. S. Lee, W. Im, *J. Comput. Chem.* **2017**, *38*, 1879.
- [27] Lindahl, Abraham, Hess, van der Spoel GROMACS 2020.1 Source code, 2020, <https://zenodo.org/record/3685919>. Accessed 12/2021.
- [28] H. J. C. Berendsen, D. van der Spoel, R. van Drunen, *Comput. Phys. Commun.* **1995**, *91*, 43.
- [29] B. Hess, C. Kutzner, D. van der Spoel, E. Lindahl, *J. Chem. Theory Comput.* **2008**, *4*, 435.
- [30] M. J. Abraham, T. Murtola, R. Schulz, S. Páll, J. C. Smith, B. Hess, E. Lindahl, *SoftwareX* **2015**, *1-2*, 19.
- [31] T. A. Wassenaar, H. I. Ingólfsson, R. A. Böckmann, D. P. Tieleman, S. J. Marrink, *J. Chem. Theory Comput.* **2015**, *11*, 2144.
- [32] L. Monticelli, S. K. Kandasamy, X. Periole, R. G. Larson, D. P. Tieleman, S.-J. Marrink, *J. Chem. Theory Comput.* **2008**, *4*, 819.
- [33] J. J. Uusitalo, H. I. Ingólfsson, S. J. Marrink, I. Faustino, *Biophys. J.* **2017**, *113*, 246.
- [34] F. Grunewald, G. Rossi, A. H. De Vries, S. J. Marrink, L. Monticelli, *J. Phys. Chem. B* **2018**, *122*, 7436.
- [35] S. O. Yesylevskyy, L. V. Schäfer, D. Sengupta, S. J. Marrink, *PLOS Comput. Biol.* **2010**, *6*, e1000810.
- [36] U. Essmann, L. Perera, M. L. Berkowitz, T. Darden, H. Lee, L. G. Pedersen, *J. Chem. Phys.* **1995**, *103*, 8577.
- [37] G. Bussi, D. Donadio, M. Parrinello, *J. Chem. Phys.* **2007**, *126*, 014101.
- [38] H. J. Berendsen, J. P. Postma, W. F. Van Gunsteren, A. Dinola, J. R. Haak, *J. Chem. Phys.* **1984**, *81*, 3684.
- [39] M. Parrinello, A. Rahman, *J. Appl. Phys.* **1981**, *52*, 7182.
- [40] T. A. Wassenaar, K. Pluhackova, R. A. Böckmann, S. J. Marrink, D. P. Tieleman, *J. Chem. Theory Comput.* **2014**, *10*, 676.
- [41] B. R. Brooks, R. E. Brucoleri, B. D. Olafson, D. J. States, S. Swaminathan, M. Karplus, *J. Comput. Chem.* **1983**, *4*, 187.
- [42] A. D. MacKerell, D. Bashford, Bellott, R. L. Dunbrack, J. D. Evanseck, M. J. Field, S. Fischer, J. Gao, H. Guo, S. Ha, D. Joseph-McCarthy, L. Kuchnir, K. Kuczera, F. T. K. Lau, C. Mattos, S. Michnick, T. Ngo, D. T. Nguyen, B. Prodhom, W. E. Reiher, B. Roux, M. Schlenkrich, J. C. Smith, R. Stote, J. Straub, M. Watanabe, J. Wiórkiewicz-Kuczera, D. Yin, M. Karplus, *J. Phys. Chem. B* **1998**, *102*, 3586.
- [43] B. R. Brooks, C. L. Brooks, A. D. Mackerell, L. Nilsson, R. J. Petrella, B. Roux, Y. Won, G. Archontis, C. Bartels, S. Boresch, A. Caflich, L. Caves, Q. Cui, A. R. Dinner, M. Feig, S. Fischer, J. Gao, M. Hodoscek, W. Im, K. Kuczera, T. Lazaridis, J. Ma, V. Ovchinnikov, E. Paci, R. W. Pastor, C. B. Post, J. Z. Pu, M. Schaefer, B. Tidor, R. M. Venable, et al., *J. Comput. Chem.* **2009**, *30*, 1545.
- [44] A. Leonard, N., R. W. Pastor, J. B. Klauda, *J. Phys. Chem. B* **2018**, *122*, 6744.
- [45] K. Vanommeslaeghe, E. Hatcher, C. Acharya, S. Kundu, S. Zhong, J. Shim, E. Darian, O. Guvench, P. Lopes, I. Vorobyov, A. D. Mackerell, *J. Comput. Chem.* **2010**, *31*, 671.
- [46] B. Hess, *J. Chem. Theory Comput.* **2008**, *4*, 116.
- [47] S. Nosé, *J. Chem. Phys.* **1984**, *81*, 511.
- [48] S. Nosé, *Mol. Phys.* **1984**, *52*, 255.
- [49] W. G. Hoover, *Phys. Rev. A* **1985**, *31*, 1695.
- [50] W. Humphrey, A. Dalke, K. Schulten, *J. Mol. Graph.* **1996**, *14*, 33.
- [51] T. Williams, C. Kelley, D. Crawford Gnuplot 5.2: An interactive plotting program, 2019, <http://gnuplot.sourceforge.net/>. Accessed 12/2021.
- [52] M. Seeber, M. Cecchini, F. Rao, G. Settanni, A. Caflich, *Bioinformatics* **2007**, *23*, 2625.
- [53] N. Michaud-Agrawal, E. J. Denning, T. B. Woolf, O. Beckstein, *J. Comput. Chem.* **2011**, *32*, 2319.
- [54] R. Gowers, M. Linke, J. Barnoud, T. Reddy, M. Melo, S. Seyler, J. Domański, D. Dotson, S. Buchoux, I. Kenney, O. Beckstein, in *Proc. 15th Python Science Conference, SciPy*, **2016**, pp. 98–105, <http://mdanalysis.org>.
- [55] I. Radford, A. Fersht, G. Settanni, *J. Phys. Chem. B* **2011**, *115*, 22.
- [56] O. H. Ollila, G. Pabst, *Biochim. Biophys. Acta - Biomembr.* **2016**, *1858*, 2512.
- [57] O. H. Samuli Ollila, M. S. Miettinen Matching lipid force fields with NMR data, <http://nmrlipids.blogspot.fi/>. Accessed 12/2021.